SALT WELDING DURING CANOPY ADVANCE AND SHORTENING IN THE GREEN CANYON AREA, NORTHERN GULF OF MEXICO

Turki K. Alshammasi*, Sian L. Evans[¤], Christopher A-L. Jackson[#µ]

Basins Research Group (BRG), Department of Earth Science & Engineering, Imperial College, Prince Consort Road, London, SW7 2BP, UK

**Present address: Saudi Aramco, Dhahran 31311, Kingdom of Saudi Arabia*

[¤] *Present address: Department of Geosciences, University of Oslo, Sem Sælands vei 1, Oslo, 0316, Norway*

[#]*Present address: Department of Earth and Environmental Sciences, The University of Manchester, Williamson Building, Oxford Road, Manchester, M13 9PL, UK*

[µ]email: Christopher.jackson@manchester.ac.uk

Abstract

Welds form due to tectonically-induced thinning and/or dissolution of salt, with their composition and completeness thought to at least partly reflect their structural position within the salt-tectonic system. Despite their importance as seals or migration pathways for accumulations of hydrocarbons and CO_2, we have relatively few published examples of drilled subsurface welds; such examples would allow us to improve our understanding of the processes and products of welding, and to test analytical models of the underlying mechanics. In this study we integrate 3D seismic reflection and borehole data from the Green Canyon Area of the northern Gulf of Mexico, USA to characterize the geophysical and geological expression of a tertiary weld, as well as its broader salt-tectonic context. These data show although it appears complete on seismic reflection data, the weld contains 124 ft (c. 38 m) of pure halite. This thickness is consistent with the predictions of analytical models, and with observations from other natural examples of subsurface welds. Our observations also support a model whereby compositional fractionation of salt occurs as the salt-tectonic system evolves; in this model, less mobile and/or denser units, if originally present, are typically stranded within the deeper,

autochthonous level, trapped in primary welds, or near the basal root of diapirs, whereas less viscous and/or less dense units form the cores of these diapirs and, potentially, genetically related allochthonous sheets and canopies. We also show that shearing of the weld during downslope translation of the overlying minibasin did *not* lead to complete welding.

Introduction

Salt welds form in response to the removal of salt by tectonically-induced thinning and/or dissolution (e.g., Jackson and Cramez, 1989; Rowan, 2004; Wagner & Jackson, 2011; Jackson et al., 2014; 2018; Jackson & Hudec, 2017). We can identify three main types of welds depending on the structural level (i.e., autochthonous or allochthonous) at which they occur in a salt-tectonic system; (i) *primary*; (ii) *secondary*; and (iii) *tertiary* (Fig. 1) (Jackson and Cramez, 1989). We can further classify these as *complete*, *incomplete*, or *discontinuous* based on the continuity and degree of welding (see Wagner & Jackson, 2011; see also fig. 1b in Jackson et al., 2014). The type of rock left within an apparent weld (or the incomplete parts of a discontinuous weld) principally reflects the rheological variations between more mobile evaporites (e.g., halite, potash salts) and less mobile lithologies (e.g., anhydrites, carbonates and/or clastics; Kupfer, 1968), and the position of the weld within the overall salt-tectonic system (i.e., primary, secondary, or tertiary; Fig. 1). For example, primary welds may be halite-poor because lower-viscosity, relatively mobile lithologies, such as halite, are preferentially expelled (or dissolved) before higher-viscosity, less mobile lithologies (cf. 'differential purification by movement': Kupfer 1968). In contrast, tertiary welds formed at structurally shallower levels in the salt-tectonic system may contain only the more mobile lithologies, such as halite, with less mobile lithologies, if originally present at the autochthonous level, stranded at depth (Fig. 1). In cases where the autochthonous salt is very pure and comprises almost exclusively mobile lithologies such as halite and potash salt, for example towards the basin centre (e.g., Clark et al., 1998; Jackson et al., 2019), welds developed at *all* structural levels will comprise only those lithologies. In other words, compositional fractionation (or differential purification by movement) will not occur because there is nothing to fractionate.

Regardless of structural level and weld composition, analytical models show that viscous flow alone is rarely sufficient to produce a complete weld (Wagner and Jackson, 2011). In this case, up to 50 m of salt may remain within the weld, a prediction supported by the very few studies

of natural subsurface salt welds (Jackson et al., 2014; 2018). Wagner and Jackson (2011) argue that the remaining salt must be removed by dissolution. However, they also propose that viscous flow with a shear component, for example due to the horizontal translation of a supra-salt minibasin onto and along base-salt relief, may promote the complete removal of salt from a weld (Fig. 2). To date, however, relatively simple models linking salt weld composition and structural position, and analytical model-based predictions of weld thickness, have only rarely been directly tested by data from natural examples of exposed or subsurface salt welds (Jackson et al., 2014; 2018).

Understanding the composition and thickness of salt welds is critically important to the hydrocarbon industry (Rowan, 2004; Rowan et al., 2012) and those wishing to store CO_2 in sub-salt reservoirs. Halite typically has very low permeability and can therefore act as a regional or local seal for hydrocarbons or CO_2. However, welds may act as conduits for fluid migration if they are relatively thin and/or composed of non-halite lithologies (e.g., intra-salt sandstone or carbonate stringers; Jackson et al., 2014). Understanding when a weld forms in relation to the timing of hydrocarbon migration is also important, given welding needs to occur before sub-salt source rock expulsion to charge a supra-salt trap (Peel, 2014). In the region of the Gulf of Mexico that is the focus of this study, hydrocarbons are found within minibasins at various levels within the salt-tectonic system, both below and above allochthonous salt, meaning it is also important to understand the role of salt welds in controlling hydrocarbon migration within this particular region, with notable hydrocarbon fields in the vicinity including K2/K2-North, Marco Polo, Genghis Khan, Shenzi/Shenzi North, Mad Dog, and Atlantis (McBride et al., 1998; Mount et al., 2006; Weimer et al., 2017). At present, however, there is no clear way to predict if a weld is complete or incomplete due to the lack of well penetrations, limited seismic resolution, and the poor preservation of some evaporite rock-types (e.g., halite) in the field (e.g., La Popa Basin, Mexico; Rowan et al., 2012; Flinders Range, Australia; Dyson and Rowan, 2004; Hearon et al., 2014; onshore Texas, US; Willis et al., 2001).

In this study, we integrate 3D seismic reflection and borehole data from the Green Canyon area of the northern Gulf of Mexico, USA to characterize the geophysical and geological expression of an apparent tertiary salt weld (Fig. 3). The weld underlies an c. 8.5 km thick minibasin that subsided into allochthonous salt forming part of the Sigsbee Canopy. Although the weld appears complete on seismic reflection data, our borehole-based analysis shows 124 ft (c. 38

m) of pure halite is preserved (i.e., the weld is incomplete, at least at the borehole location, and may be best-classified as discontinuous). This thickness is consistent with the analytical model-based predictions of Wagner & Jackson (2011), and observations from other natural examples of subsurface salt welds (Jackson et al., 2014; 2018). By studying the structural evolution of the overlying minibasin and flanking salt structures, we also place the weld within its broader salt-tectonic framework, showing that shearing of the weld during downslope translation of the overlying minibasin (see Fig. 1) did *not* lead to complete welding, at least in the location penetrated by the borehole.

Geological Setting

The northern Gulf of Mexico initially formed in the Late Triassic-Early Jurassic in response to rifting between the North American and African-South American plates (e.g., Pindell and Dewey, 1982; Kneller and Johnson, 2011; Hudec et al., 2013a). Terrestrial clastic-dominated syn-rift sediments were overlain by a thick, extensive, evaporite-dominated succession known as the Louann Salt, which was previously considered to be Callovian (e.g., Salvador, 1987), but that is now dated as Bajocian (Pindell et al., 2019) (see also Hazzard et al., 1947; Humphris, 1978; Kneller and Johnson, 2011; Hudec et al., 2013b). The main Louann-Campeche salt basin was dissected by opening of the central Gulf of Mexico in the earliest Late Jurassic. During the Late Jurassic and Early Cretaceous, the salt flowed out over newly formed oceanic crust in the evolving ocean basin, forming an extensive, frontal allochthonous nappe (Hudec et al 2013a,b) that underlies our study area. Subsequent gravity-driven flow of these evaporites during the Cenozoic played a primary role in the structural evolution of the Gulf of Mexico and the distribution of overlying sediments. Minibasins subsided into both the autochthonous and allochthonous salt, while salt flowed out of diapiric feeders and formed an allochthonous salt layer known as the Sigsbee Canopy (e.g., Diegel et al., 1995; Peel et al., 1995; Rowan, 1995; Pilcher et al., 2011). As this canopy advanced basinward during the Oligocene to Miocene, a new generation of minibasins subsided into and were transported broadly south/south-eastwards on top of the advancing allochthonous body (see Fig. 2a) (e.g., Jackson et al., 2010; Jackson and Hudec, 2017). Previous studies suggest that these minibasins were carried tens of kilometres basinward before welding, being flanked updip and downdip by kinematically linked zones of salt-detached extension and contraction, respectively (Fig. 2; see also fig. 20 in Jackson et al., 2010; Duffy et al., 2020). The presence of ramp-syncline basins in this part

of the Sigsbee Canopy also provide evidence for at least 40 km of salt-detached minibasin translation across base-salt relief (Fernandez et al., 2021).

The salt weld of interest in this study is a tertiary weld located below a minibasin that has subsided into the Sigsbee Canopy, and which appears welded to an underlying minibasin. This minibasin is situated in the Green Canyon Area of the northern Gulf of Mexico, USA and close to the frontal edge of the advancing canopy (the Sigsbee Escarpment), whose expression can be clearly seen in the present bathymetry (Fig. 3). In a salt tectonic context, the studied minibasin and underlying weld lie within the 'amalgamated salt-stock-canopy province' of Pilcher et al. (2011), the upper part of which is characterised by a network of minibasins surrounded by canopy-sourced diapirs and related welds (Fig. 1b).

Data and methods

Seismic reflection data and seismic-stratigraphic framework

We use a 3D pre-stack depth migrated (PSDM) seismic reflection volume that covers c. 150 km^2 (12.5 x 12 km), and which has an inline and crossline spacing of 20 m (Figs 3 and 4). The available data volume is cropped at a depth of 23,760 ft (7,200 m) from a survey that images to significantly greater depth. Seismic data quality is very good within the interval of interest, with the weld and encasing strata being very well-imaged (Fig. 5). We estimate the vertical seismic resolution within the depth interval at which the weld is developed (c. 20,000 ft; c. 6.1 km) to be c. 62 ft (c. 20 m) (resolution is approximated by the assumption that it equals $\lambda/4$, where λ=80 m at 20,000 ft). We display the seismic data using US normal polarity (i.e., a downward increase in acoustic impedance is represented by a negative reflection coefficient, which is a white reflection event in our images; Brown, 2011) (Fig. 5).

We mapped eight key seismic horizons comprising top and base salt, and six supra-salt seismic horizons that define six seismic units (SU1-6; Figs 4a-c, 5 and 6). The six supra-salt horizons are defined based on seismic-stratigraphic terminations, such as onlaps and erosional truncations (Fig. 5). We use thickness (isochore) maps and stratigraphic relationships to determine the tectonic evolution of the minibasin (Figs 4, 5 and 7). Note that we measure stratal thickness vertically, rather than orthogonal to bedding, i.e., we generate isochore rather than

isopach maps. This means that the stratal thicknesses displayed in our isochore maps may be slightly overestimated in the case of moderately dipping (<25°) strata (i.e., as observed in SU1; see below). However, we quality-control our maps with observations from seismic reflection profiles, ensuring that the observed thickness patterns, which are critical for our interpretation of the salt-tectonic evolution of the study area, are not simply an artefact of our seismic interpretation method. The ages of the horizons, which span the Miocene to Recent, are directly constrained (i.e., top SU3 and SU6) or estimated (i.e., top SU1-2 and SU4-5) from biostratigraphic data obtained from a borehole penetrating the central, thickest part of the minibasin and its underlying weld (Figs 4b-d, 5e and 6). Our age-constrained seismic-stratigraphic framework is important because it enables us to determine the timing and duration of the major salt-tectonic events, including the potential timing of welding.

Borehole data

We use data from a borehole drilled in a water depth of c. 4,200 ft (1,300 m) to a total depth of 30,803 ft (9,389 m). Available datasets include well-logs, mud-logs, biostratigraphic, and operational reports. Well-logs cover the interval 4,235-21,422 ft (1,290-6,529 m), which includes the studied weld (Fig. 6). Well-logs include gamma ray (gAPI), sonic (μs/ft), density (g/cm^3), neutron (ft^3/ft^3), caliper (in) and deep resistivity (ohm-m) (Fig. 4). We used data from these well-logs to determine weld lithology and thickness, which helped understand its sealing potential. These logs also helped constrain the lithology of material above and below the weld, which was critical when considering its seismic expression at and lateral to the borehole location. Biostratigraphic samples span 10,920-22,300 ft (3,328-6,797 m) and were examined by the borehole operator and partners at 30 ft (9.1 m) increments. Because these data are confidential, we report here only the key geological age boundaries (Fig. 6).

Salt-tectonic structure

Base-salt relief

The allochthonous salt forming the Sigsbee Canopy salt overlies a reflective, clastic-dominated, Late Jurassic to Miocene succession, the uppermost of which is Tortonian-to-earliest Messinian (i.e., Late Miocene; Figs 5 and 6). The base of the Sigsbee salt is rugose,

consisting of a prominent, NW-trending, steeply SW-dipping ramp (c. 30º) that is at least 5000 ft (1,524 m) long, with relief of at least 2000 ft (609 m) (Figs 4a, 4d, 5a and 5d). North of this ramp, base-salt dips gently (c. 3º) to the WNW, although low-relief rugosity of a few hundred metres is also locally observed in this area (Figs 4a, and 5a-b). Where the base-salt reflection lies beneath the seismic reflection volume, such as in the west of the study area, we infer the presence of a diapiric feeder that provided salt to the Sigsbee Canopy (Pilcher et al., 2011; Jackson et al., 2018) (Figs 4a, 4d and 5e). As we will discuss below, base-salt relief, in particular the NW-trending ramp and the local structural high it delineates, are important controls on the structural development of the supra-salt minibasin.

Distribution and thickness of allochthonous salt

The salt thickness varies considerably across the study area. It appears locally welded in the middle of the study area, where it has been expelled from beneath a large minibasin (Figs 4b-d and 5). In detail, the weld is discontinuous, comprising areas of (apparently) complete welding and small, elongate, wall-like pockets of salt that are up to 3750 ft (1,143 m) thick and 2000 ft wide (Figs 4b and 5). Some of these pockets occur in the footwall of salt-detached, intra-minibasin thrusts (Figs 5a and 5b) or at the base of sub-vertical welds (Fig. 5d) (see below). Thick (locally up to 21,724 ft or 6,621m), diapiric salt seemingly encircles the minibasin.

Supra-salt minibasin

The supra-salt minibasin contains Serravallian (Middle Miocene) to Holocene deep-water clastics (Fig. 6). It is important to note that the strata directly above the weld are older (Serravallian) than the strata directly underlying it (Messinian) (c. 20300 ft; Fig. 6); we discuss the significance of this observation below. The geometry of the top salt surface (Fig. 4), and thickness changes in its lowermost part (Fig. 4c), indicate the studied minibasin is, at least in its lower part, composed of at least seven smaller, broadly bowl-shaped sub-basins (labelled A-G; Fig. 4d; see also Fig. 5). These sub-basins are separated by salt-detached thrusts that have pockets of salt preserved in their footwall (see above; Fig. 5a and b) or sub-vertical welds (Figs 3b, 3d and 5d). These thrusts show highly variable strikes (i.e., N-S to ENE-WSW) and dips (i.e., W to SSE), but we note that they are restricted to the northern side of the base-salt ramp

and its related structural high (Fig. 5d). All salt-detached thrusts are flanked by hangingwall anticlines and footwall synclines, and are overlain by unbreached monoclines, which we interpret as fault-propagation folds (Fig. 5a-c). Strata within the lower sub-basins *and* within the overlying, larger, singular minibasin, thin towards and onlap onto flanking diapirs (most clearly seen in Fig. 5d-e; see also 5a-b). We provide a more detailed description of the minibasins seismic-stratigraphic patterns below.

Supra-salt minibasin seismic stratigraphy and evolution

Vertical changes in seismic-stratigraphic patterns and stratal thickness (Figs 5 and 6) suggest the studied minibasin initially comprised at least seven sub-basins and underwent six main stages of structural development. We describe and interpret these sub-basins and related stages below (see Fig. 10), using the age-constrained seismic-stratigraphic framework (Fig. 6) to constrain their timing and duration.

Stage 1 (Serravallian-Messinian)

The thickness map of SU1 shows at least seven distinct sub-basins (A-F and H; Fig. 7a). The sub-basins contain broadly bowl- to locally wedge-shaped seismic packages (Fig. 5). Strata within these packages onlap the large, flanking diapirs and the pockets of salt locally preserved beneath the minibasin (Fig. 5).

Based on these observations we interpret that the minibasin was initially comprised of seven smaller minibasins that independently subsided symmetrically and sub-vertically (where containing bowl-shaped packages), or slightly asymmetrically (where containing wedge-shaped packages) into the allochthonous salt canopy during a phase of passive diapirism (Fig. 10A and B) (e.g., Rowan & Weimer, 1999; Jackson et al., 2019). There is strong evidence that these early minibasins were located updip (i.e., north) of their present location and were translating basinward (i.e., broadly southward) above the advancing salt canopy (Fig. 10A and B). This interpretation is supported by the observation that the minibasin is: (i) bound updip and downdip by zones of extension and contraction, respectively, suggesting it lies within a domain that has undergone lateral translation (see Jackson et al., 2010; see also Duffy et al., 2020); and (ii) spatially related to ramp-syncline basins that record at least 40 km of horizontal

translation (Fernandez et al., 2020). This interpretation also explains the age repetition observed above the weld, which suggests this supra-salt section cannot have been deposited *in situ*; i.e., whilst Serravallian and Messinian sediments were being deposited at the base of the minibasin, sediment of a similar age were being deposited downdip, in an area that was not yet covered by the advancing salt canopy or ultimately, the supra-salt minibasin.

Stage 2 (Messinian)

In contrast to SU1, which defined seven sub-basins, depocentres within SU2 define only four sub-basins; a relatively large, bowl-shaped depocentre centred on the borehole (an amalgamation of sub-basins A, D and E) and two smaller sub-basins located to the north (sub-basin B, and sub-basins C and F, which are now linked; Fig. 7b). Strata within these sub-basins still onlap the large diapirs flanking the host minibasins although they do not onlap intra-minibasin diapirs, which were buried by strata within the upper part of SU1 (Fig. 5). Instead, SU2 thins across, and the larger minibasin is segmented by, fault-related folds above the upper tips of intra-minibasin thrusts forming the boundary between, for example, sub-basins B and A (Fig. 5a), B and C (Fig. 5b), C and D (Fig. 5b), and A and E (Fig. 5a).

These seismic-stratigraphic relationships indicate that the intra-minibasin thrusts became active, and thus that the causal shortening initiated in the Messinian (see also Figs 7b and 10C). We suggest that the low-relief diapirs that previously separated sub-basins defined by SU1 were squeezed and the sub-basins collided to form steeply dipping thrust welds, with small pockets of the salt beneath these welds representing remnant diapir pedestals (Figs 5d-e and 10C). The origin of this shortening is unclear. A possible interpretation is that downdip (i.e., sub-basin E; Fig. 4D) and updip sub-basins collided due to welding of the former against the gently NW-dipping, base-salt ramp as it translated downdip. We currently reject this interpretation, however, given that shortening and thrusting clearly occurred during the very early stages of minibasin development, when the depocentre was relatively thin (i.e., c. 30% of its eventual total thickness; Fig. 10C) and presumably surrounded and underlain by thick salt (Figs 4C and 5). It is thus unlikely that shallow minibasins, riding on thick salt, would weld at this time. Instead, we tentatively suggest that early shortening was induced by a more regional event occurring outside of the immediate study area, such as large-scale obstruction of the southwards advancing Sigsbee Canopy by aggrading sediment on the abyssal plain. In this case, the downdip sub-basin (i.e., sub-basin E; Fig. 4D) may have decelerated and been collided

into by the still-translating, updip sub-basins (i.e., sub-basins A and D; Fig. 4D), even if it had not welded (Fernandez et al., 2020). However, we cannot determine this definitively with the available dataset.

Stage 3 (Messinian-Piacenzian)

SU3 lies conformably above SU2 but is capped by a major angular unconformity that truncates underlying reflections (Fig. 5). Although influenced by the capping erosional surface (Fig. 5), thickness patterns within SU3 clearly differ to those observed in SU1 and SU2. First, only two main depocentres are defined; (i) a broadly NE-trending depocentre north of the borehole spanning sub-basins C, F, and the northern part of A; and (ii) a sub-circular depocentre spanning sub-basins B and G (Figs 5 and 7c). Second, these thickness patterns are less obviously controlled by intra-minibasin thrusts or diapirs. Stratigraphic thinning above and onlap onto thrust-related folds are locally observed at the base of SU3, although the faults do not propagate up into this unit. The thrust-related folds also die-out upwards towards the top of SU3, such that the uppermost, youngest strata bury underlying relief and are largely undeformed.

These observations suggest that thrusting continued into the earliest Piacenzian, implying intra-minibasin shortening was ongoing (the origin of which was unclear; see above), but that it had slowed and ultimately ceased by the late Piacenzian to Gelasian (Fig. 10C). Uplift associated with the shortening and tilting of the minibasin, combined with an influx of sediment across the evolving canopy, may have led to the development of the erosional unconformity capping SU3 (not shown in Fig. 10).

Stage 4 (Gelasian-Pleistocene)

SU4 displays overall thickening towards the NW. However, in the northern part of the study area we observe two sub-circular depocentres (Fig. 7D), related to the filling of erosional relief developed along the top Pliocene erosional unconformity (see Fig. 5B). SU4 also differs to SU2 and SU3 in that it is dominated by broadly layer-/weakly wedge-shaped seismic packages that overstep and cap the minibasin-flanking diapirs (Fig. 5). Most critically, however, SU4 shows no thickness changes with respect to the intra-minibasin thrust-related folds, indicting the minibasin was less segmented, and was subsiding as a single, large depocentre by the

Gelasian (Figs 5, 7D and 10D). This also supports the interpretation that intra-minibasin shortening has ceased by the Gelasian. There is, however, syn-depositional thickening in the footwall of a newly developed thrust fault at the NE margin of the minibasin (Fig. 5c and 5d). This fault has a low-displacement (<50 m), dips NE, strikes NW-SE, and has an arcuate geometry in plan-view (Fig. 4d).

The dominance of areally extensive, layer-shaped, diapir-capping packages indicates passive diapirism had ceased at this time, possibly due to weld-induced termination of salt supply to the flanking diapirs (see Rowan and Weimer, 1989; Jackson et al., 2019). Given that the supra-salt minibasin was travelling broadly southward and by this time was relatively thick, we interpret that shortening was driven by welding against the gently WNW-dipping flank of the base-salt ramp (Fig. 10C) (e.g., Duffy et al., 2020). This interpretation is also supported by the orientation (i.e., broadly ramp-parallel), position (i.e., on the updip side of the minibasin), and dip direction (i.e., the same as the dip of the ramps low-angle flank) of the shallow thrust, i.e., as a minibasin becomes obstructed, a local contractional zone may develop behind it as the updip overburden continues to push against it (Duffy et al., 2020).

The shift in depocentre toward the NW, combined with the weakly wedge-shaped seismic packages observed in similarly trending seismic profiles (Fig. 5a and 5b), suggests that the minibasin was also tilting broadly north-westwards at this time (Fig. 10D). This tilting of the minibasin could result from differential active rise of the flanking diapirs (Fig. 10D) (Fernandez et al. 2020). Further minibasin shortening, tilting, and related salt evacuation may also have been associated with continued development of the weld (Ge et al., 2020).

Stage 5 (Late Pleistocene-Holocene?)

SU5 comprises broadly tabular packages of sub-parallel reflections that locally thin towards flanking diapirs at the minibasin margins, but which invariably cap these structures (Figs 5 and 7e). Growth strata and erosional truncation of the uplifted hangingwall indicate continued slip on the structurally shallow, salt-detached thrust at the NE minibasin margin (Fig. 5c-d).

The dominance of layer-shaped seismic packages across the study area suggests minibasin subsidence had ceased and aggradation above the now-welded depocentres continued (Rowan and Weimer, 1998; Jackson et al., 2019). However, thinning of strata within SU5 towards

flanking diapirs suggests these structures continued to actively rise, possibly in response to ongoing shortening within the canopy. This shortening may have been accommodated in the overburden by the shallow-level thrusts (Figs 5a, 5b and 10E).

Stage 6 (Late Pleistocene-Holocene?)

SU6 defines a NW-trending depocentre characterised by broadly layer-shaped seismic packages that cap and show only moderate thickness changes within respect to minibasin-flanking diapirs (Figs 5 and 7f). Based on this seismic-stratigraphic architecture, which is crudely like that observed in SU5, we suggest the latest Pleistocene to Holocene was characterised by only minor salt tectonics (e.g., minibasin subsidence and/or diapir rise), and dominated by deep-water sediment aggradation (Fig. 10E).

Salt weld thickness and composition

The salt-bearing interval penetrated by the borehole (i.e., the weld) is characterised by anomalously low gamma ray values (c. 24 gAPI), high density (2.4-2.95 g/cm^3), low neutron porosity (-0.5-0.2 pu.), high resistivity (c. 10^3), low sonic slowness (c. 68 s/ft) (i.e., it has a high p-wave velocity) (Figs 8 and 9). We note there is some scatter in these values, particularly in terms of density and sonic slowness (i.e., velocity), an observation we discuss further below. Based on these criteria, we confidently picked, stratigraphically rather than seismically, top salt at 20255 ft (6174 m) and base-salt at 20379 ft (6212 m), interpreting that the (apparent) weld is 124 ft (38 m) thick and dominated by halite (Fig. 9) (Rider and Kennedy, 2011; Jackson et al., 2014, 2018). Mudlogging reports are consistent with our well-log-based interpretation, describing only halite from this approximate depth interval. However, we also note that the halite is: (i) denser (by c. 0.4-1 g/cm^3) than ideal values (Rider and Kennedy, 2011) and values documented from elsewhere in the northern Gulf of Mexico for this rock type (Jackson et al., 2018); and (ii) acoustically faster (by sonic slowness values of c. 20-40 us/ft) than values documented from elsewhere in the northern Gulf of Mexico for this rock type (Jackson et al., 2018). We explore the potential reasons for this in the Discussion.

INTERPRETATION AND DISCUSSION

Age and salt-tectonic context of the salt weld and related canopy

Previous regional studies suggest canopy emplacement in this area of the northern Gulf of Mexico occurred during the Middle–Late Miocene in response to regional shortening and the related extrusion of salt from diapiric feeders (Peel et al. 1995). Using 3D seismic reflection and borehole data, Jackson et al. (2018) interpret that the majority of canopy emplacement in the Atwater Valley area, c. 100 km to the ENE of our study area, was in fact considerably later, sometime in the Early Pleistocene. Our observation that the weld (and laterally equivalent salt structures forming the canopy) studied here is immediately underlain by late Miocene (Messinian) strata suggests canopy emplacement in the late Miocene, consistent with the age originally proposed by Peel et al. (1995). Given that we use seismic reflection data of a broadly similar vintage and, we infer, quality to that of Jackson et al. (2018), we propose that the difference in *local* canopy emplacement reflects *regional* diachroneity in the timing of emplacement, rather than dataset quality (i.e., borehole data are of sufficient resolution to constrain the age of sub- and suprasalt rocks and, thus, the timing of canopy emplacement; see Jackson et al. 2018). More specifically, this diachroneity might reflect systematic changes in the timing of: (i) sediment loading-driven evacuation of salt from the deep, Mesozoic nappe to the shallower, Sigsbee Nappe; and/or (ii) regional shortening-driven squeezing of diapirs that then fed salt to the canopy. For example, feeders in the Atwater Valley area of Jackson et al. (2018) may have been shortened and expelled salt later than elsewhere, meaning the canopy advanced into this area only after a period of latest Miocene and Pliocene sediment aggradation. An alternative interpretation is that evacuation rates, whether load- or shortening-driven, were regionally synchronous, but that locally higher sediment accumulation rates in the Atwater Valley area meant that salt breakout and canopy advance were delayed by aggrading sediment in flanking minibasins.

The stratigraphic repetition observed in the borehole (i.e., Serravallian strata overlying *younger* Messinian across an incomplete salt weld) most likely results from the downslope translation of the minibasin within an evolving canopy. We interpret that deep-water sedimentation within the developing minibasin commenced in the Serravallian when the structure was located some distance upslope to the north. Ahead of the advancing canopy and overlying minibasin, sediment of the same age continued aggrading within underlying minibasins up until the Messinian. As a result, an age repetition occurred when the minibasin translated over and welded to the underlying minibasin (e.g., Duffy et al., 2020; Fernandez et al., 2020).

Canopy dynamics and related welding also controlled minibasin structural style by driving thrusting and folding (Fig. 10C). Contractional structures such as these are common on salt-detached slopes, forming when minibasins collide due to; (i) a mobile minibasin colliding with a slower-moving, welded or otherwise obstructed minibasin (*sensu* Duffy et al., 2020); or (ii) two mobile minibasins colliding due to ongoing shortening (Jackson et al., 2008; Duffy et al., 2021). In the former case, the contractional structures most commonly develop during the latter stages of minibasin development, once minibasins become thick enough to touch down on the base-salt surface, thus welding and forming an obstruction. This is typically associated with the squeezing (and in some cases eventual secondary welding) of intervening diapirs, which readily explains the formation of the relatively young thrust and related secondary weld at a relatively shallow level on the NE margin of the studied minibasin (Fig. 5C, D). As the minibasin migrated southwards it eventually welded to the low-relief flank of the base-salt ramp. In contrast, the relatively old contractional structures observed at the base of the minibasin might not have formed due to welding, but may instead record a more regional salt-tectonic event and the related collision of translating minibasins (Fernandez et al., 2020). Additional regional data, for example seismic reflection and borehole data to constrain the kinematic history of adjacent minibasins, are required to test this hypothesis.

Geological, geophysical, and petrophysical expression of welds and implications for the process of welding

Although they are readily imaged in seismic reflection data from a range of salt-tectonic settings, there are relatively few published examples of salt welds penetrated by boreholes. Such data are required to determine the completeness, composition, and petrophysical expression of the weld and encasing wall rocks. Jackson et al. (2014) show that a primary weld in the Santos Basin, offshore Brazil is *incomplete* (*sensu* Wagner, 2010; Wagner and Jackson, 2011), containing 22 m of carbonate, anhydrite, sandstone, and marl, with halite absent. A tertiary weld in the Atwater Valley area of the northern Gulf of Mexico is also incomplete; however, rather than being halite-poor, this c. 24 m thick weld is halite-dominated and contains a 4 m-thick mudstone inclusion (Jackson et al., 2018). Although data remain sparse, current observations of salt composition and thickness are consistent with a model whereby compositional fractionation of salt occurs as the salt-tectonic system evolves, i.e. more viscous, less mobile and/or denser units are typically stranded within the deeper, autochthonous level, trapped in primary welds, or stranded near the basal root of diapirs, whereas less viscous and/or

less dense units form the cores of these diapirs and, potentially, genetically related allochthonous sheets and canopies (Fig. 1) (cf. 'differential purification by movement': Kupfer 1968; see also Wagner & Jackson 2011; Jackson et al. 2014; 2018). Current data are also consistent with the predictions of analytical and numerical models presented by Wagner & Jackson (2011), which suggest natural salt welds formed by viscous flow alone may contain anywhere from ≪1 m to up to c. 50 m of remnant salt. Viscous flow may therefore be a good analytical approximation of the physical processes occurring during salt thinning and welding; viscous flow alone is unlikely, however, to result in complete evacuation of salt.

Our borehole data from the northern Gulf of Mexico allow us to further test and refine these related models for salt welding during the development of multi-level salt-tectonic systems. Our data indicate that the seismically imaged tertiary weld is *incomplete* (i.e., it is an "apparent weld"; *sensu* Jackson et al., 2014*)*, being defined by c. 124 ft (38 m) of remnant evaporitic rocks (i.e., halite). This thickness is slightly more than previously documented in the Santos Basin (Jackson et al., 2014) and elsewhere in the northern Gulf of Mexico (Jackson et al., 2018), but is consistent with the analytical model-based prediction of welding via viscous flow (Wagner and Jackson, 2011). The halite has a very clear expression in well-log data, being characterised by relatively very low radioactivity (as expressed in gamma-ray log data), and high density, velocity (i.e., low acoustic slowness), and resistivity. However, as noted above; (i) our cross-plot of halite density and velocity displays some scatter (Fig. 9); and (ii) the halite is denser than ideal values for this rock type (Rider and Kennedy, 2011) and values documented from natural halite penetrated elsewhere in the northern Gulf of Mexico for this rock type (Jackson et al., 2018), and acoustically faster than values documented from elsewhere in the northern Gulf of Mexico (Jackson et al., 2018). The former observation might suggest the halite could be slightly impure due to the presence of disseminated grains or thin laminae of denser and acoustically faster (e.g., carbonate), or less dense and acoustically slower (e.g., siliciclastic) material; we infer that this effect, if present, is only very minor, given that the halite retains very different petrophysical properties to that of encasing clastic rocks (Fig. 9). Determining why the halite is denser and acoustically faster is more challenging, but it might reflect the fact that different logging tools and drilling approaches (e.g., drilling fluids) were used to acquire the data in the different boreholes.

Notwithstanding its slightly unusual petrophysical expression, the occurrence of only halite within the tertiary weld is at least consistent with a model of rheologically-controlled compositional fractionation, i.e., the less mobile units (e.g., clastic, carbonate, or anhydrite rocks) remain at the deeper, autochthonous level, trapped in primary welds, whereas more

mobile units (e.g., halite, potash salts) flow into diapiric salt structures and canopies, thus dominating salt composition at the allochthonous level (Fig. 1). As such, when allochthonous salt welds, we suggest these secondary and tertiary welds will be relatively enriched in halite and possibly potash salts, as opposed to halite-poor primary welds. This is the case in the example presented here, although we note that the compositional variability encountered in salt welds will also likely reflect several factors such as compositional variations in the autochthonous salt or preferential dissolution of more soluble salts (e.g., halite and potash salts). For example, primary, secondary, and tertiary welds will *all* be halite-bearing if only halite was present at the autochthonous level; such a case may arise in the very distal parts of salt basins, basinward of the pinchout of anhydrite, as well as non-evaporite rock types (e.g., Clark et al., 1998; Jackson et al., 2019).

Why is there salt left in the weld?

Two main processes control the evacuation and removal of salt in a weld; dissolution and solid-state flow (Jackson and Hudec, 2017). We do not think dissolution played a role in salt thinning and/or was able to fully remove the remaining salt from the weld due to the weld being buried >1 km (around 3,300 ft); at such depths sluggish water flow is anticipated, limiting dissolution, even if a large amount of NaCl-undersaturated water is present (Jackson and Hudec, 2017). Welding by solid-state flow is more plausible, although Wagner and Jackson (2011) use analytical solutions to show that viscous flow alone cannot fully remove salt from a weld due to boundary drag along the perfectly flat and parallel, upper and lower contacts. Because of this process, they suggest that 1-50 m (3–165 ft) of residual salt will remain in a weld, a range consistent with the thickness of salt observed here (38 m), and in welds in the Santos Basin, Brazil (22 m; Jackson et al., 2014) and elsewhere in the northern Gulf of Mexico (24 m; Jackson et al., 2018).

Borehole and field data demonstrate complete welding is at least locally possible along incomplete welds (Rowan et al., 2012; Jackson and Hudec, 2017). Based on analytical models, Wagner and Jackson (2011) hypothesize that shear-thinning could lead to the complete removal of salt from a weld. Our interpreted structural evolution based on seismic-stratigraphic analysis and borehole data suggests that the basal weld of the studied minibasin has been sheared. More specifically, the presence of squeezed diapirs, and thrusts and related secondary welds in the lower parts of the minibasin suggests horizontal shortening, part of which we infer occurred after the minibasin had welded onto an upslope-dipping, base-salt ramp. Despite this, the weld

is incomplete, at least at the borehole location, suggesting insufficient shearing had occurred to fully remove all the salt from a weld.

Implications for hydrocarbon exploration and the storage of CO_2

Salt has relatively low permeability and can therefore form a high-quality seal to underlying or laterally adjacent accumulations of hydrocarbons or CO_2 (e.g., Warren, 2016). The precise sealing properties of salt are at least partly dictated by its thickness and composition, i.e., all other things being equal, a relatively thin (<10 m), incomplete, halite-dominated tertiary weld may be a better seal than a thicker primary weld dominated by carbonate and clastic rocks. In the region of the northern Gulf of Mexico considered here, giant hydrocarbon fields, sourced from sub-salt source rocks, underlie, and are presumably at least partly sealed by, Sigsbee salt (e.g., K2/K2-North, Genghis Khan, Shenzi/Shenzi North, Mad Dog, and Atlantis). However, smaller supra-salt fields (e.g., Marco Polo; Weimer et al., 2017), also fed by sub-salt source rocks, are also present within this region, suggesting: (i) complete welds are present locally beneath the canopy; and/or (ii) incomplete welds can leak. These observations, in combination with the data presented here, point to a complex relationship between salt composition, salt-tectonic structural development, salt weld properties, and petroleum systems development, with related implications for the entrapment of CO_2. Predictive models for the evolution and physical properties of salt welds, such as the differential purification by movement-model outlined above, require further development and testing by existing and new borehole data.

Conclusions

We used 3D seismic reflection and borehole data from the Green Canyon Area of the northern Gulf of Mexico, USA to characterize the geophysical and geological expression, and the regional salt-tectonic structural context of a tertiary salt weld. The weld is developed at the base of a minibasin that likely translated seaward in allochthonous salt of the Sigsbee Canopy, before colliding with and welding to a base-salt ramp. Welding and the related collision of otherwise mobile minibasins led to at least two phases of shortening, both of which were associated with the development of salt-detached thrusts and folds, and secondary welds. The seaward translation and eventual welding of the minibasin also led to an across-weld stratigraphic repetition, with Serravallian strata overlying younger Messinian strata. Our petrophysical analysis of borehole data showed that although it appears *complete* on seismic

reflection data, and although it may have undergone some shortening-related shearing, the basal weld is in fact *incomplete*, containing 124 ft (c. 38 m) of pure halite. This thickness is consistent with observations from other natural examples of subsurface welds, and with the predictions of analytical models of welding by viscous flow. Our observations support a model in which compositional fractionation of salt occurs as the salt-tectonic system evolves; in this model, less mobile and/or denser units are typically stranded within the deeper, autochthonous level, trapped in primary welds, or stranded near the basal root of diapirs, whereas less viscous and/or less dense units form the cores of these diapirs and, potentially, genetically related allochthonous sheets and canopies. More studies of drilled subsurface welds are required to assess the processes (i.e., mechanics) and products of salt welding, and the role they play in the trapping of hydrocarbons and the storage of CO_2.

Acknowledgements

We thank BHP for permission to use and show their proprietary seismic and borehole data, and Schlumberger for providing Petrel software to Imperial College via an Academic License Agreement. We thank Ryan Lewis, Neil Evans, Erik Peterson, Kanetra Moses, Rody Alzona, and Tom Hider for facilitating data access and transfer, and for general support of our research. Oliver Duffy, Naiara Fernandez, and Mike Hudec are also thanked for very helpful discussions during this study. Frank Peel and Keny Ge provided excellent reviews that helped improve the manuscript.

References

Brown, A.R. 2011. Interpretation of three-dimensional seismic data, 7th edition. AAPG Memoir, 42/SEG Investigations in Geophysics, 9, pp315.

Clark, J.A., Stewart, S.A., & Cartwright, J. 1998. Evolution of the NW Margin of the North Permian Basin, UK North Sea. Journal of the Geological Society, 155, 663–676.

Diegel, F.A., Karlo, J.F., Schuster, D.C., Shoup, R.C. and Tauvers, P.R. 1995. Cenozoic structural evolution and tectono-stratigraphic framework of the northern Gulf Coast continental margin. In: Jackson, M.P.A., Roberts, D.G. & Snelson, S. (eds) Salt Tectonics: A Global Perspective. AAPG Memoir, 65, 109–151.

606
607 Duffy, O.B., Fernandez, N., Peel, F.J., Hudec, M.R., Dooley, T.P. and Jackson, C.A.-L. 2020.
608 Obstructed minibasins on a salt-detached slope: An example from above the Sigsbee canopy,
609 northern Gulf of Mexico. Basin Research, 32, 505-524.
610
611 Duffy, O.B., Dooley, T.P., Hudec, M.R., Fernandez, N., Jackson, C.A.-L. and Soto, J.I. (in
612 press). Principles of Shortening in Salt Basins Containing Isolated Minibasins. Basin Research.
613
614 Dyson, I.A. and Rowan, M.G. 2004. Geology of a welded diapir and its flanking minibasins in
615 the Flinders Ranges of South Australia. Proceedings of GCSSEPM Foundation 24th Annual
616 Bob F. Perkins Research Conference, 390–403.
617
618 Fernandez, N., Hudec, M.R., Jackson, C.A.L., Dooley, T.P. and Duffy, O.B. 2020. The
619 competition for salt and kinematic interactions between minibasins during density-driven
620 subsidence: observations from numerical models. Petroleum Geoscience, 26, 3-15.
621
622 Fernandez, N., Duffy, O.B., Peel, F.J. and Hudec, M.R. 2021. Influence of minibasin
623 obstruction on canopy dynamics in the northern Gulf of Mexico. Basin Research, 33, 427-446.
624
625 Ge, Z., Gawthorpe, R.L., Rotevatn, A., Zijerveld, L., Jackson, C.A-L. and Oluboyo, A. 2020.
626 Minibasin depocentre migration during diachronous salt welding, offshore Angola. Basin
627 Research, 32, 875-893.
628
629 Hazzard, R.T., Spooner, W.C. and Blanpied, B.W. 1947. Notes on the stratigraphy of the
630 formations which underlie the Smackover Limestone in south Arkansas, northeast Texas, and
631 north Louisiana. In: Shreveport Geological Society Reference Report on Certain Oil and Gas
632 Fields of North Louisiana, South Arkansas, Mississippi and Alabama, Volume II. Shreveport
633 Geological Society, Shreveport, IL, USA, 483–503.
634
635 Hearon, T.E., IV, Rowan, M.G., Lawton, T.F., Hannah, P.T. and Giles, K.A. 2014. Geology
636 and tectonics of Neoproterozoic salt diapirs and salt sheets in the eastern Willouran Ranges,
637 South Australia. Basin Research, 27, 183-207.
638

639 Hudec, M.R., Jackson, M.P.A. and Peel, F.J. 2013a. Influence of deep Louann structure on the
640 evolution of the northern Gulf of Mexico. AAPG Bulletin, 97, 1711-1735.
641
642 Hudec, M.R., Norton, I.O., Jackson, M.P.A. and Peel, F.J. 2013b. Jurassic evolution of the
643 Gulf of Mexico salt basin. AAPG Bulletin, 97, 1683–1710.
644
645 Humphris, C.C., Jr. 1978. Salt movement on continental slope, northern Gulf of Mexico. In:
646 Bouma, A.H., Moore, G.T. & Coleman, J.M. (eds) Framework, Facies, and Oil-Trapping
647 Characteristics of the Upper Continental Margin. AAPG Studies in Geology, 7, 69–86.
648
649 Jackson, C.A.-L., Rodriguez, C.R., Rotevatn, A. and Bell, R.E. 2014. Geological and
650 geophysical expression of a primary salt weld: An example from the Santos Basin, Brazil.
651 Interpretation, 2, SM77-SM89.
652
653 Jackson, C.A.-L., Zhang, Y., Herron, D.A. and Fitch, P. 2018. Subsurface expression of a salt
654 weld, Gulf of Mexico. Petroleum Geoscience, 25, 102-111.
655
656 Jackson, C.A-L., Elliott, G.M., Royce-Rogers, E., Gawthorpe, R.L. and Aas, T.E. 2019. Salt
657 thickness and composition influence rift structural style, northern North Sea, offshore Norway.
658 Basin Research, 31, 514-538.
659
660 Jackson, C.A.-L., Duffy, O.B., Fernandez, N., Dooley, T.P., Hudec, M.R., Jackson, M.P.A.
661 and Burg, G. 2020. The stratigraphic record of minibasin subsidence, Precaspian Basin,
662 Kazakhstan. Basin Research, 32, 739-763.
663
664 Jackson, M.P.A. and Cramez, C. 1989. Seismic recognition of salt welds in salt tectonics
665 regimes: Gulf of Mexico salt tectonics, associated processes and exploration potential: Gulf
666 Coast Section-SEPM Foundation 10th Annual Research Conference, 66-71.
667
668 Jackson, M.P.A, Hudec, M.R., Jennette, D.C. and Kilby, R.E. 2008. Evolution of the
669 Cretaceous Astrid thrust belt in the ultradeep-water Lower Congo Basin, Gabon. AAPG
670 Bulletin, 92, 487-511.
671

672 Jackson, M.P.A, Hudec, M.R. and Dooley, T.P. 2010. Some emerging concepts in salt tectonics
673 in the deepwater Gulf of Mexico: intrusive plumes, canopy-margin thrusts, minibasin triggers
674 and allochthonous fragments. In: Vining, B.A. and Pickering, S.C. (eds) Petroleum Geology:
675 From Mature Basins to New Frontiers—Proceedings of the 7th Petroleum Geology
676 Conference, 899-912.
677
678 Jackson, M.P.A. and Hudec, M.R., 2017. Salt tectonics: Principles and Practice. Cambridge
679 University Press.
680
681 Kneller, E.A. and Johnson, C.A. 2011. Plate kinematics of the Gulf of Mexico based on
682 integrated observations from the Central and South Atlantic. Gulf Coast Association of
683 Geological Societies Transactions, 61, 283–300.
684
685 McBride, B.C., Weimer, P. and Rowan, M.G. 1998. The effect of allochthonous salt on the
686 petroleum systems of northern Green Canyon and Ewing Bank (offshore Louisiana), northern
687 Gulf of Mexico. AAPG Bulletin, 82, 1083-1112.
688
689 Mount, V. S., Rodriguez, A., Chaouche, A., Crews, S.G., Gamwell, P. and Montoya, P. 2006.
690 Petroleum system observations and interpretation in the vicinity of the K2/K2-North, Genghis
691 Khan, and Marco Polo fields, Green Canyon, Gulf of Mexico. Gulf Coast Association of
692 Geological Societies Transactions, 56, 613-625.
693
694 Peel, F.J. 2014. How do salt withdrawal minibasins form? Insights from forward modelling,
695 and implications for hydrocarbon migration. Tectonophysics, 630, 222-235.
696
697 Peel, F.J., Travis, C.J. and Hossack, J.R. 1995. Genetic structural provinces and salt tectonics
698 of the Cenozoic offshore U.S. Gulf of Mexico: A preliminary analysis. In: Jackson, M.P.A.,
699 Roberts, D.G. & Snelson, S. (eds) Salt Tectonics: A Global Perspective. AAPG Memoir, 65,
700 153–175.
701
702 Pindell, J. and Dewey, J.F. 1982. Permo-Triassic reconstruction of western Pangea and the
703 evolution of the Gulf of Mexico/Caribbean region. Tectonics, 1, 179–211.
704

Pilcher, R.S., Kilsdonk, B. and Trude, J. 2011. Primary basins and their boundaries in the deep-water northern Gulf of Mexico: Origin, trap types, and petroleum system implications. AAPG Bulletin, 95, 219-240.

Rider, M. and Kennedy, M. 2011. The geological interpretation of well logs, 3rd edition. Rider-French Consulting Limited.

Rowan, M.G. 1995. Structural styles and evolution of allochthonous salt, central Louisiana outer shelf and upper slope. In: Jackson, M.P.A., Roberts, D.G. & Snelson, S. (eds) Salt Tectonics: A Global Perspective. AAPG Memoir, 65, 199–228.

Rowan, M.G. 2004. Do salt welds seal? In: Post, P.J., Olson, D.L., Lyons, K.T., Palmes, S.L. Harrison, P.F. & Rosen, N.C. (eds) Salt–Sediment Interactions and Hydrocarbon Prospectivity: Concepts, Applications, and Case Studies for the 21st Century. Proceedings of the GCSSEPM Foundation 24th Annual Bob F. Perkins Research Conference. GCSSEPM Foundation, Austin, TX, USA, 390–403.

Rowan, M.G. and Weimer, P., 1998. Salt-sediment interaction, northern Green Canyon and Ewing bank (offshore Louisiana), northern Gulf of Mexico. AAPG Bulletin, 82, 1055-1082.

Rowan, M.G., Lawton, T.F. and Giles, K.A. 2012. Anatomy of an exposed vertical salt weld and flanking strata La Popa Basin, Mexico. In: Alsop, G.I., Archer, S.G., Hartley, A.J., Grant, N.T. & Hodgkinson, R. (eds) Salt Tectonics, Sediments and Prospectivity. Geological Society, London, Special Publications, 363, 33–57.

Rowan, M.G. and Vendeville, B.C. 2006. Foldbelts with early salt withdrawal and diapirism: Physical model and examples from the northern Gulf of Mexico and the Flinders Ranges, Australia. Marine and Petroleum Geology, 23, 871-891.

Wagner, B.H., III. 2010. An analysis of salt welding. PhD dissertation, University of Texas at Austin, Austin, TX, USA.

Wagner III, B.H. and Jackson, M.P.A. 2011. Viscous flow during salt welding. Tectonophysics, 510, 309-326.

Warren, J.K., 2016, Evaporites: A Compendium. Springer, Berlin, pp.1854.

Weimer, P., Bouroullec, R., Adson, J. and Cossey, S.P. 2017. An overview of the petroleum systems of the northern deep-water Gulf of Mexico. AAPG Bulletin, 101, 941-993.

Willis, J.J., Lock, B.E., Cornell, K.C. and Rudberg, D.A. 2001. An exposed evaporite weld and related deformational structures, Edwards Plateau, I-10 corridor, Kerrville Junction-Sonara area, Texas. Transactions of the Gulf Coast Association of Geological Societies, 51, 389–396.

Figures captions

Fig. 1. Schematic cross section (not to scale) illustrating the three main types of salt weld that can develop in salt-tectonic basins. This classification is based on the structural level at which salt evacuation occurs (i.e. deep, intermediate, and shallow), the attitude of the weld (i.e. sub-horizontal or sub-vertical), and the origin of the weld (i.e. thinning of autochthonous or allochthonous salt, or squeezing and closure of a diapir) (modified from Jackson et al., 2014; see also Jackson and Cramez, 1989). The pie-charts schematically illustrate the inferred proportion of three main evaporite-related rock types that may be encountered in a primary, secondary, and tertiary welds. Note the upwards increase in halite and relative enrichment in other rock types due to “differential purification by movement” (*sensu* Kupfer, 1968). See text, and Jackson et al. (2014 and 2018) for full discussion.

Fig. 2. (a) Schematic cross section showing a minibasin translating along the top of an extruding salt sheet (Time 1). As the minibasin translates, its base impinges on a sub-salt ramp, forming a fault weld (Time 2). This natural geometry minimizes the limitations of boundary drag and promotes nearly complete welding by viscous flow alone (modified from Wagner and Jackson, 2011). (b) Schematic diagram highlighting the formation of a complete fault weld, which forms if shear displacement occurs before, during or after salt evacuation. Concepts and terminology after Jackson and Cramez (1989), Hossack and McGuinness (1990), and Rowan et al. (1999), Wagner and Jackson (2011). Modified from Wagner and Jackson (2011).

Fig. 3. Seafloor bathymetry map of the northern Gulf of Mexico and the Sigsbee canopy. The study area is located on the mid-to-lower slope. Bathymetry map sourced from the Bureau of

Ocean Energy Management (https://marinecadastre.gov/nationalviewer). Black lines show offshore protraction areas. Inset shows broader geographical location of bathymetry data.

Fig. 4. Maps illustrating the salt-tectonic structure of the study area. (a) base-salt depth; (b) top-salt depth; (c) salt isochore (thickness); and (d) interpretative sketch map showing the spatial relationship of the key salt-tectonic structures identified in (a), (b), and (c). The locations of the seismic profiles in Fig. 5 are shown. Note the thrust and related secondary weld in the NE of the study area are at a shallower structural level than those found elsewhere; see Fig. 5c and d.

Fig. 5. Interpreted seismic reflection profiles showing the salt-tectonic structure of the study area, and the structural context and seismic expression of the studied salt weld and its encasing strata. The locations of the profiles are shown in Fig. 4, and the geological ages of the sub- and suprasalt seismic-stratigraphic units (SUs) are shown in Fig. 6. Uninterpreted seismic reflection profiles are available in Supplementary Material.

Fig. 6. Simplified stratigraphic column showing key well-log information and the petrophysical expression of the main, biostratigraphically age-constrained seismic-stratigraphic units (SUs) penetrated in the borehole. The location of Fig. 8 is shown. Circled numbers on the left of the column show the borehole diameter.

Fig. 7. Isochore (thickness) maps showing temporal changes in minibasin depocentre location because of canopy advance, salt welding, and minibasin shortening and tilting. (a) SU1 – Serravallian-Messinian; (b) SU2 - Messinian; (c) SU3 – Messinian-Piacenzian; (d) SU4 – Gelasian-Pleistocene; (e) SU5 – Late Pleistocene-Holocene(?); and (f) SU6 - Late Pleistocene-Holocene(?). The position of the base-salt ramp (e.g., Fig. 5a; see also text for description and interpretation) is indicated in (a)-(c). The key intra-minibasin, sub-basin-bounding structures inferred to be active during the deposition of the Serravallian-Messinian (SU1), Messinian (SU2), and Messinian-Piacenzian (SU3) are shown; the approximate positions of these structures are inferred from their present locations as shown in Fig. 4d. Key for structures is shown in Fig. 4d. (A-H) in (a) are sub-basins described in the text and shown in Figs 4d and 5.

Fig. 8. Details of the well-log data from the depth interval c. 20170-20350 ft in the borehole, illustrating the petrophysical expression and composition of the apparent salt weld and flanking

807 strata (see also Fig. 9). The location of the borehole is shown in Figs 4, 5 and 7. The colour-
808 code refers to colours shown in Fig. 6. Note that the density and neutron porosity log responses
809 are slightly offset from the base salt due to the 13 7/8-inch casing point being set just below
810 the weld.
811
812 **Fig. 9.** Density (RHOB)-sonic slowness (DT) (i.e., velocity) cross-plot of petrophysical data
813 from the depth interval shown in Fig. 8. Note the distinct expression of intra-weld halite, which
814 is characterised by significantly higher density (typically >2.4 g/cm^3) and slow sonic slowness
815 values (typically <80 us/ft) (i.e., higher velocities) than underlying or overlying clastics. The
816 range of ideal values for clean halite are shown (taken from Rider and Kennedy, 2011), as are
817 those documented by Jackson et al. (2018) from the northern Gulf of Mexico. See text for
818 discussion.
819
820 **Fig. 10.** Schematic diagram showing the general, simplified salt-tectonic evolution of the
821 studied minibasin, salt weld, and associated structures. The stages in the diagram are broadly
822 tied to the six key stages described in the text: (a) Stage 1 (Serravallian-Messinian) – minibasin
823 nucleation and translation; (b) Stage 2 (Messinian) – initial minibasin collision and depocentre
824 coalescence; (c) Stage 3 (Messinian-Piacenzian) – minor contraction and continued translation;
825 (d) Stage 4 (Gelasian-Pleistocene) – welding and renewed contraction; (e) Stage 5 and 6 (Late
826 Pleistocene-Holocene?) – minor contraction, minibasin tilting and sediment aggradation. Note
827 that minibasins A-C do not correspond to those described in the text; they are simply labelled
828 here so that their relative positions can be tracked through the stages. Note also that
829 sheet/canopy inflation is inferred to result from the squeezing of diapiric feeders (Peel et al.,
830 1995), which may lie outside of the displayed profile.

Fig. 1

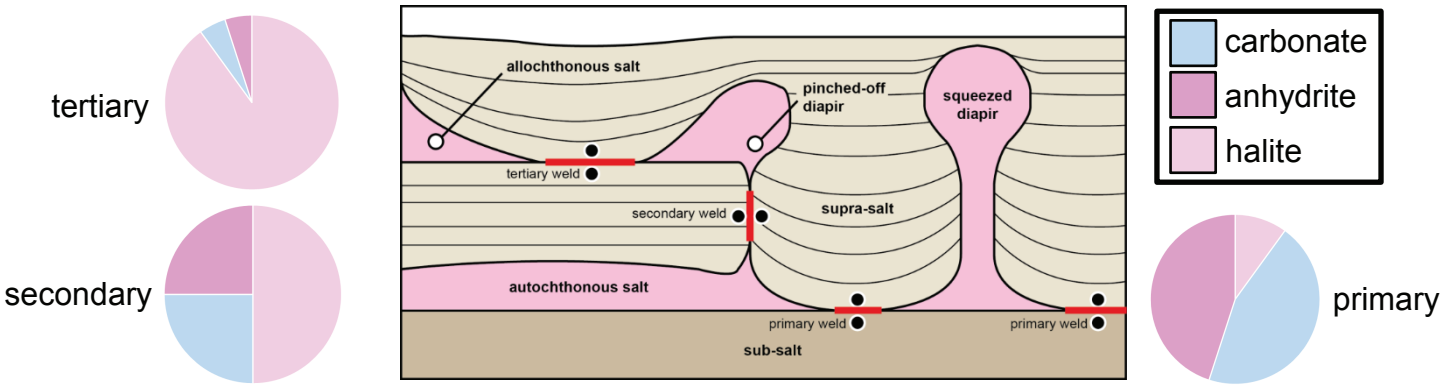

Fig. 1. Schematic cross section (not to scale) illustrating the three main types of salt weld that can develop in salt-tectonic basins. This classification is based on the structural level at which salt evacuation occurs (i.e. deep, intermediate, and shallow), the attitude of the weld (i.e. sub-horizontal or sub-vertical), and the origin of the weld (i.e. thinning of autochthonous or allochthonous salt, or squeezing and closure of a diapir) (modified from Jackson et al., 2014; see also Jackson and Cramez, 1989). The pie-charts schematically illustrate the inferred proportion of three main evaporite-related rock types that may be encountered in a primary, secondary, and tertiary welds. Note the upwards increase in halite and relative enrichment in other rock types due to “differential purification by movement” (sensu Kupfer, 1968). See text, and Jackson et al. (2014 and 2018) for full discussion.

Fig. 2

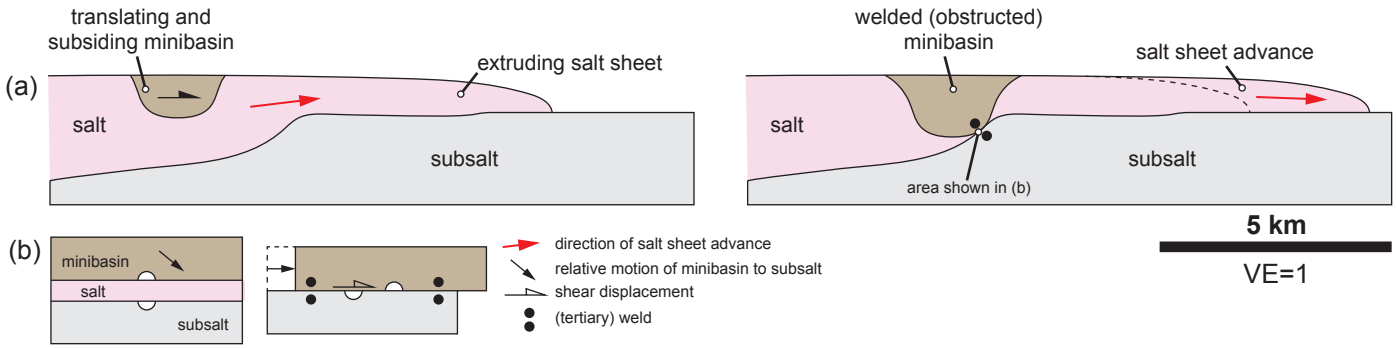

Fig. 2. (a) Schematic cross section showing a minibasin translating along the top of an extruding salt sheet (Time 1). As the minibasin translates, its base impinges on a subsalt ramp, forming a fault weld (Time 2). This natural geometry minimizes the limitations of boundary drag and promotes nearly complete welding by viscous flow alone (modified from Wagner and Jackson, 2011). (b) Schematic diagram highlighting the formation of a complete fault weld, which forms if shear displacement occurs before, during or after salt evacuation. Concepts and terminology after Jackson and Cramez (1989), Hossack and McGuinness (1990), and Rowan et al. (1999), Wagner and Jackson (2011). Modified from Wagner and Jackson (2011).

Fig. 3

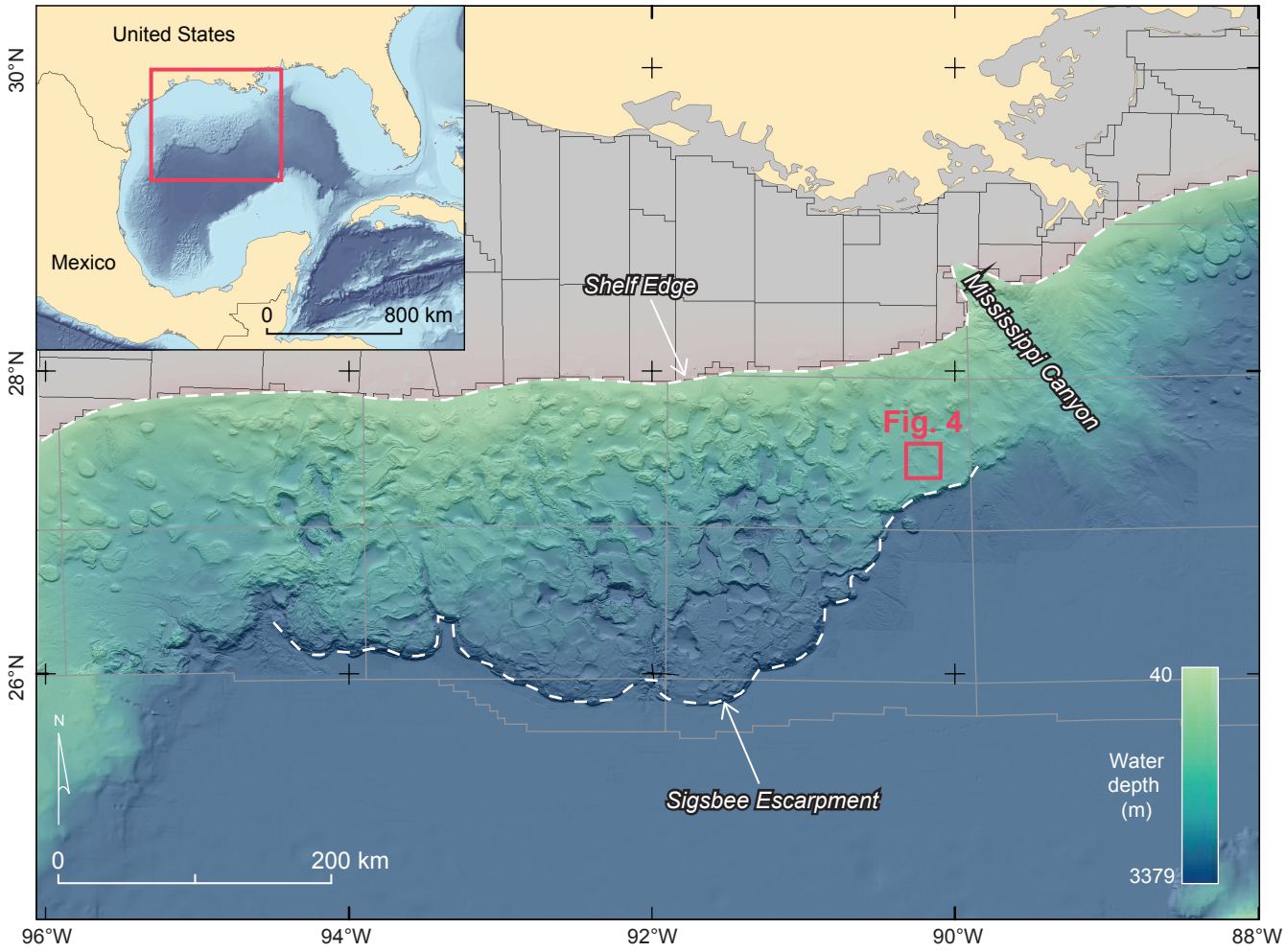

Fig. 3. Seafloor bathymetry map of the northern Gulf of Mexico and the Sigsbee canopy. The study area is located on the mid-to-lower slope. Bathymetry map sourced from the Bureau of Ocean Energy Management (https://marinecadastre.gov/nationalviewer). Black lines show offshore protraction areas. Inset shows broader geographical location of bathymetry data.

Fig. 4

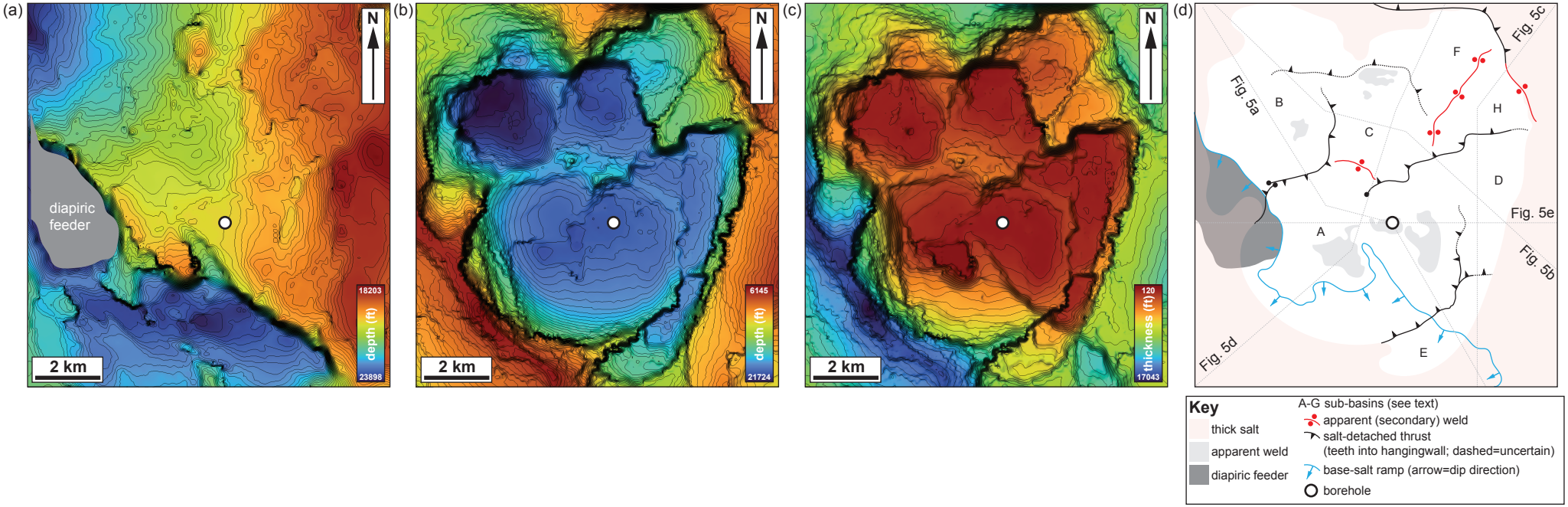

Fig. 4. Maps illustrating the salt-tectonic structure of the study area. (a) base-salt seismic horizon depth-map; (b) base-salt seismic horizon depth-map; (c) salt isopach (thickness) map; and (d) interpretative sketch map showing the spatial relationship of the key salt-tectonic structures identified in (a), (b), and (c). The locations of the seismic profiles in Fig. 5 are shown. Note the thrust and related secondary weld in the NE of the study area are at a shallower structural level than those found elsewhere; see Fig. 5c and d.

Fig. 5

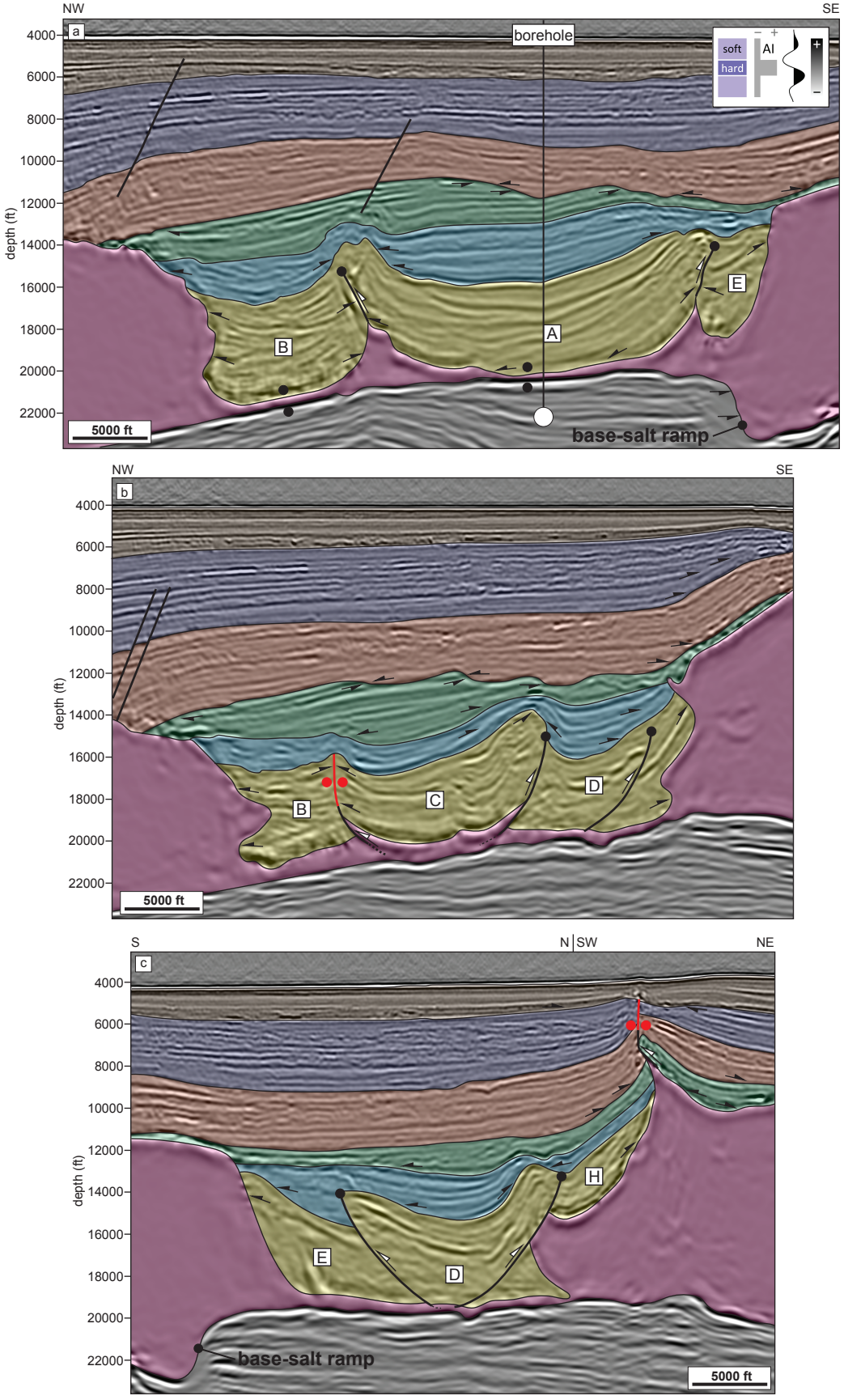
NW
SE
a
borehole
soft
hard
AI
depth (ft)
4000
6000
8000
10000
12000
14000
16000
18000
20000
22000
A
B
E
5000 ft
base-salt ramp
NW
SE
b
B
C
D
5000 ft
S
N
SW
NE
c
E
D
H
base-salt ramp
5000 ft

Fig. 5

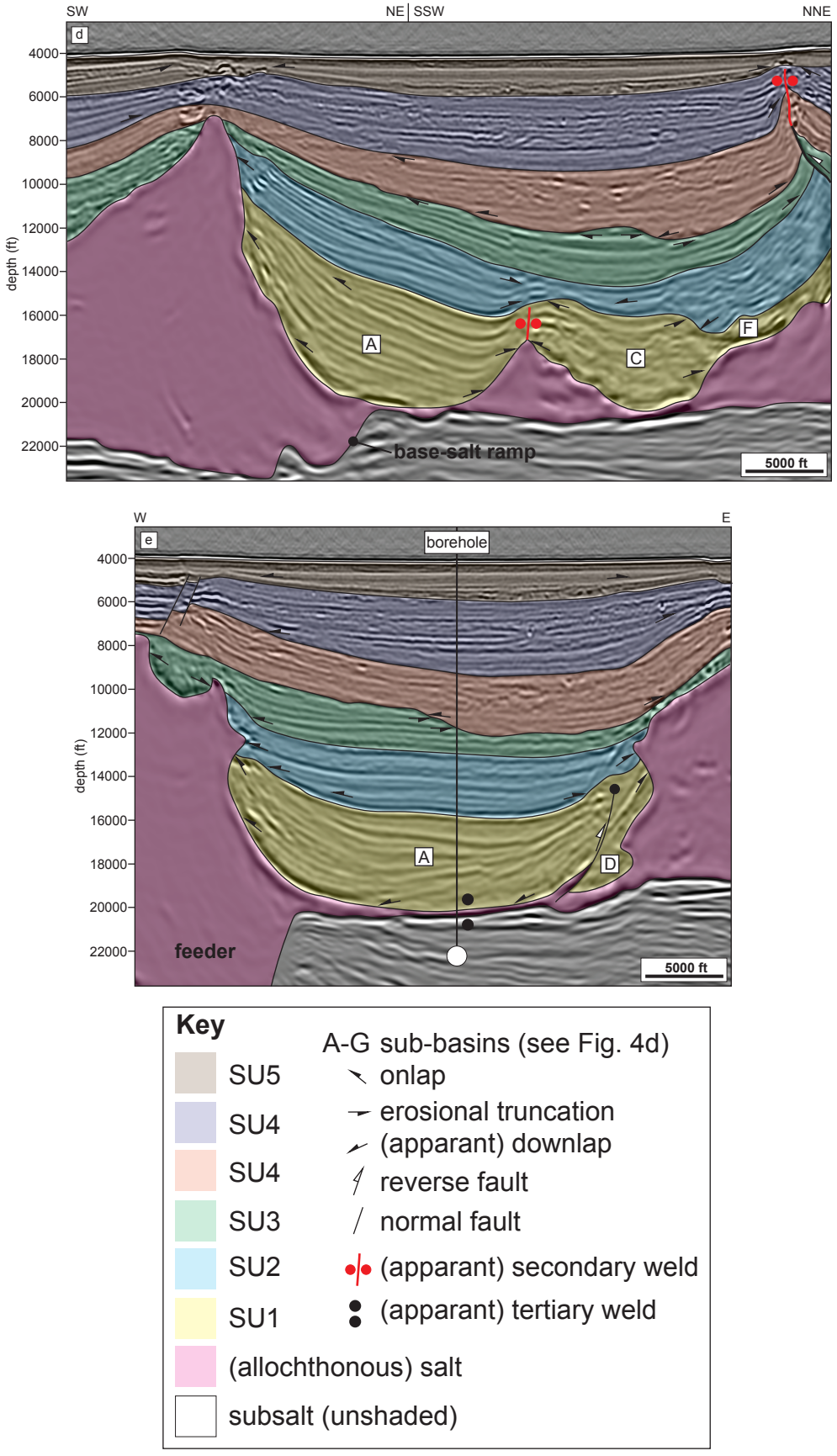

Fig. 5. Interpreted seismic reflection profiles showing the salt-tectonic structure of the study area, and the structural context and seismic expression of the studied salt weld and its encasing strata. The locations of the profiles are shown in Fig. 4, and the geological ages of the sub- and suprasalt seismic-stratigraphic units (SUs) are shown in Fig. 6. Uninterpreted seismic reflection profiles are available in Supplementary Material.

Fig. 6

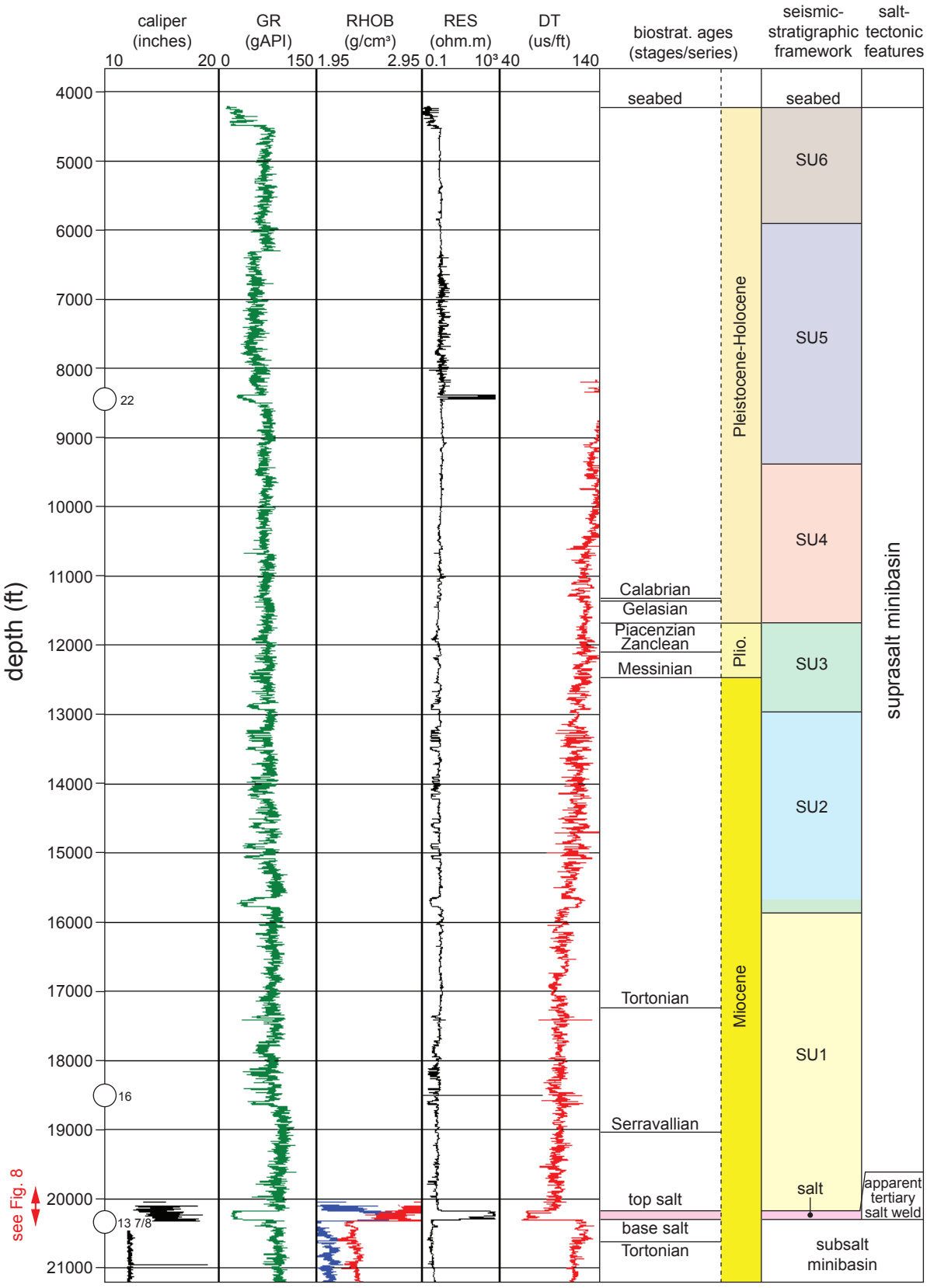

Fig. 6. Simplified stratigraphic column showing key well-log information and the petrophysical expression of the main, biostratigraphically age-constrained seismic-stratigraphic units (SUs) penetrated in the borehole. The location of Fig. 8 is shown. Circled numbers on the left of the column show the borehole diameter.

Fig. 7

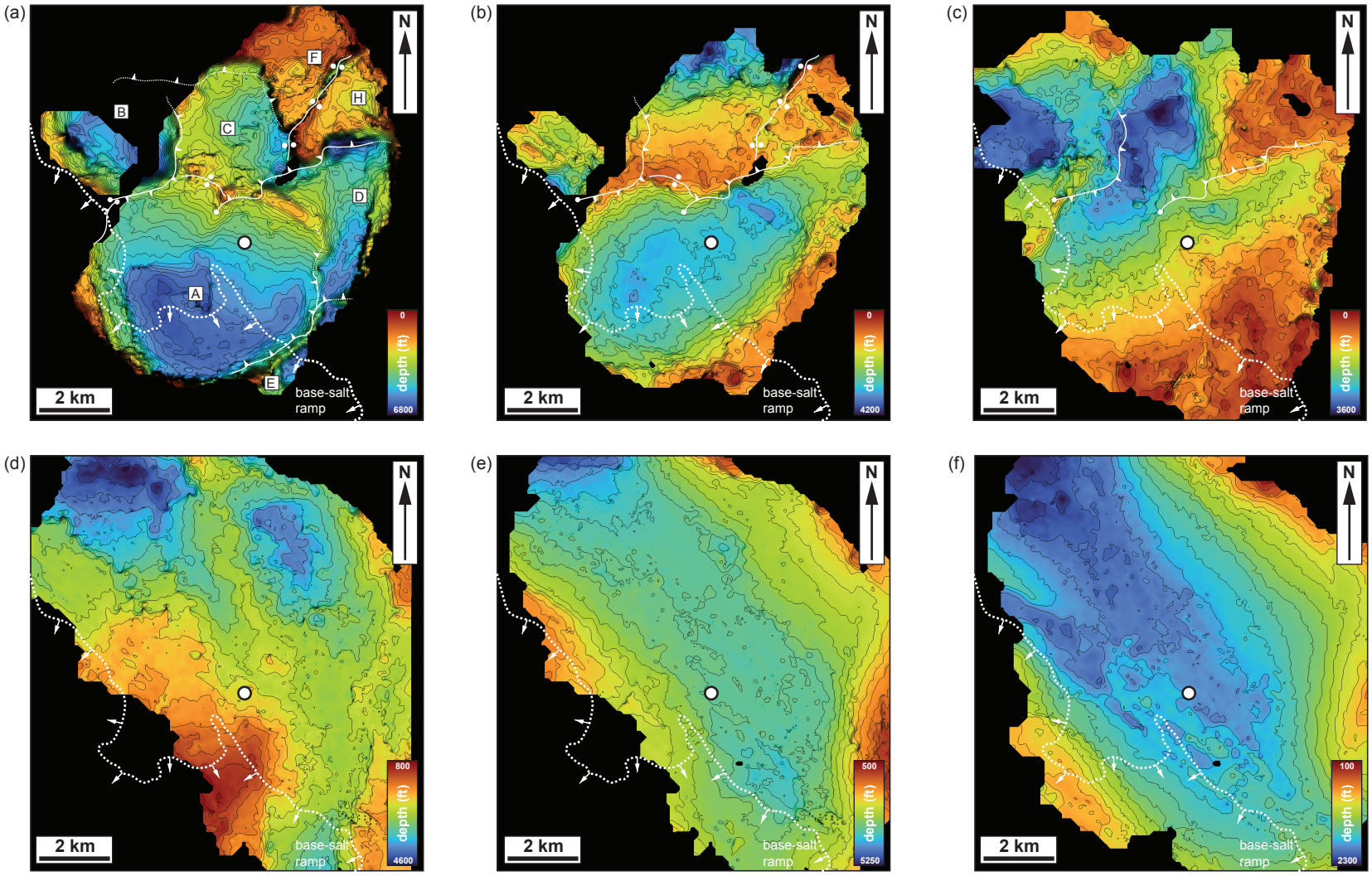

Fig. 7. Isochron (thickness) maps showing temporal changes in minibasin depocentre location because of canopy advance, salt welding, and minibasin shortening and tilting. (a) SU1 – Serravallian-Messinian; (b) SU2 - Messinian; (c) SU3 – Messinian-Piacenzian; (d) SU4 – Gelasian-Pleistocene; (e) SU5 – Late Pleistocene-Holocene(?); and (f) SU6 - Late Pleistocene-Holocene(?). The position of the base-salt ramp (e.g., Fig. 5a; see also text for description and interpretation) is indicated in (a)-(c). The key intra-minibasin, sub-basin-bounding structures inferred to be active during the deposition of the Serravallian-Messinian (SU1), Messinian (SU2), and Messinian-Piacenzian (SU3) are shown; the approximate positions of these structures are inferred from their present locations as shown in Fig. 4d. Key for structures is shown in Fig. 4d. (A-H) in (a) are sub-basins described in the text and shown in Figs 4d and 5.

Fig. 8

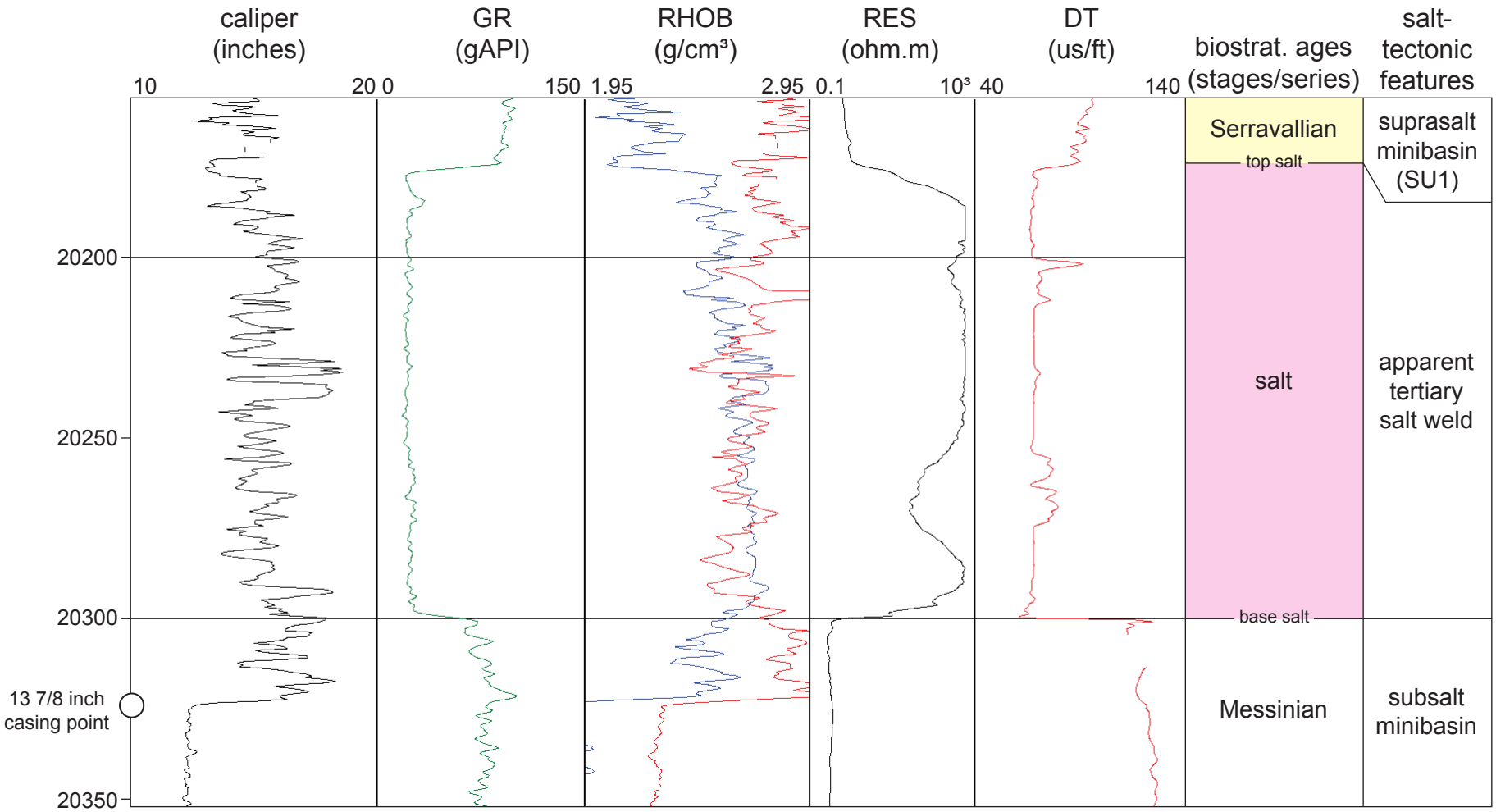

Fig. 8. Details of the well-log data from the depth interval c. 20170-20350 ft in the borehole, illustrating the petrophysical expression and composition of the apparent salt weld and flanking strata (see also Fig. 9). The location of the borehole is shown in Figs 4, 5 and 7. The colour-code refers to colours shown in Fig. 6. Note that the density and neutron porosity log responses are slightly offset from the base salt due to the 13 7/8-inch casing point being set just below the weld.

Fig. 9

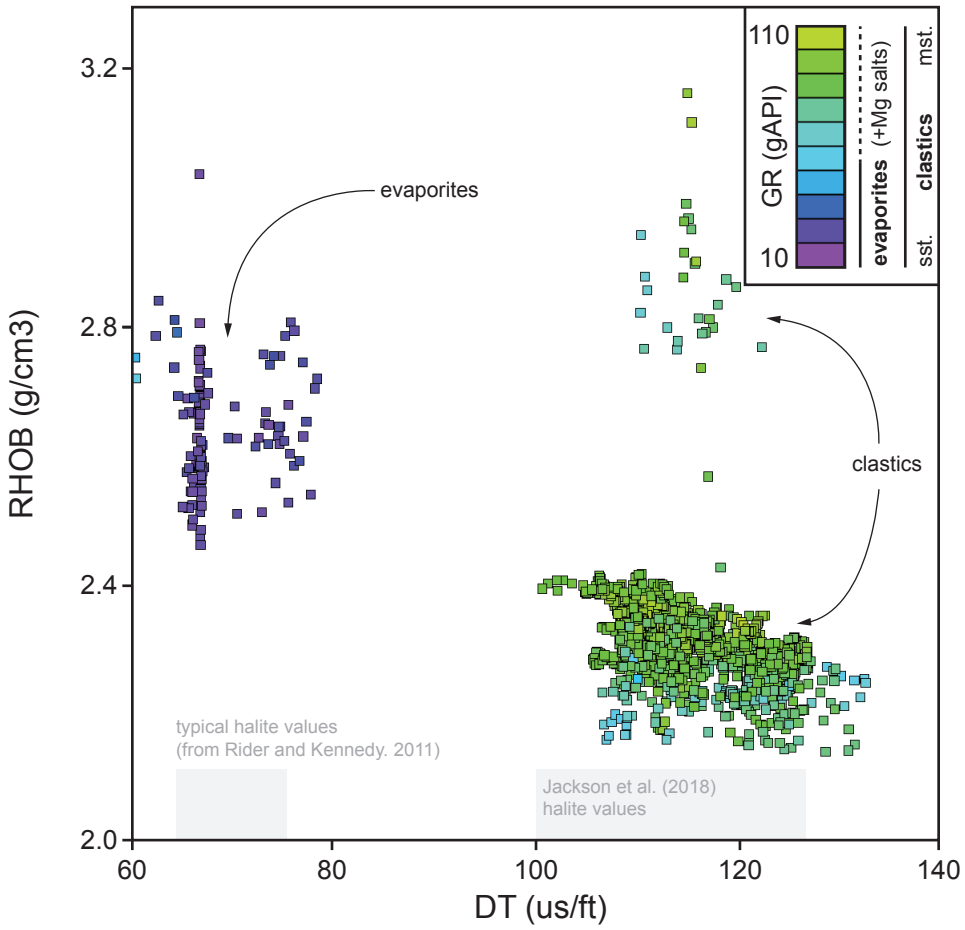

Fig. 9. Density (RHOB)-sonic slowness (DT) (i.e., velocity) cross-plot of petrophysical data from the depth interval shown in Fig. 8. Note the distinct expression of intra-weld halite, which is characterised by significantly higher density (typically >2.4 g/cm3) and slow sonic slowness values (typically <80 us/ft) (i.e., higher velocities) than underlying or overlying clastics. The range of ideal values for clean halite are shown (taken from Rider and Kennedy, 2011), as are those documented by Jackson et al. (2018) from the northern Gulf of Mexico. See text for discussion.

Fig. 10

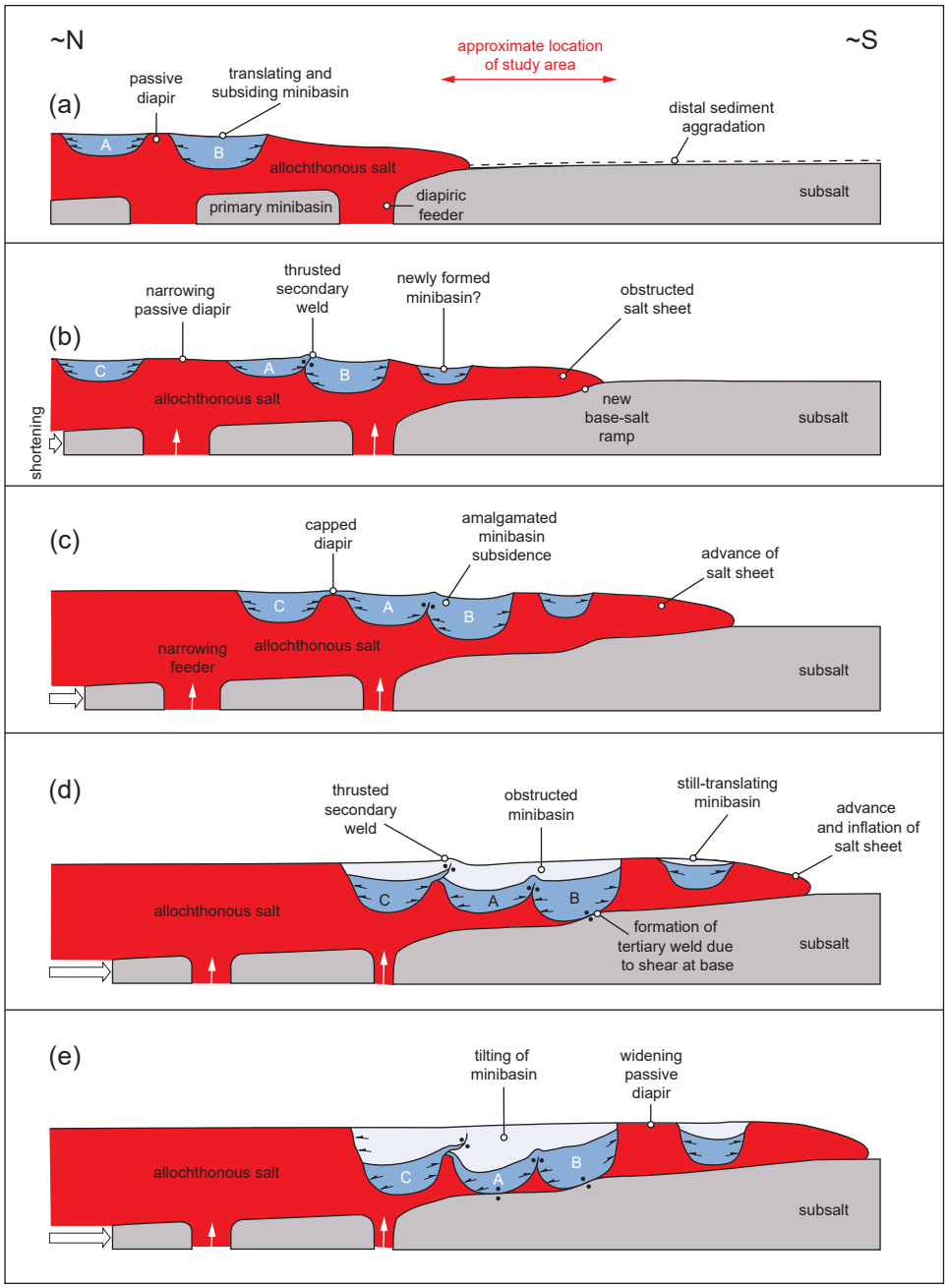

Fig. 10. Schematic diagram showing the general, simplified salt-tectonic evolution of the studied minibasin, salt weld, and associated structures. The stages in the diagram are broadly tied to the six key stages described in the text: (a) Stage 1 (Serravallian-Messinian) – minibasin nucleation and translation; (b) Stage 2 (Messinian) – initial minibasin collision and depocentre coalescence; (c) Stage 3 (Messinian-Piacenzian) – minor contraction and continued translation; (d) Stage 4 (Gelasian-Pleistocene) – welding and renewed contraction; (e) Stage 5 and 6 (Late Pleistocene-Holocene?) – minor contraction, minibasin tilting and sediment aggradation. Note that minibasins A-C do not correspond to those described in the text; they are simply labelled here so that their relative positions can be tracked through the stages. Note also that sheet/canopy inflation is inferred to result from the squeezing of diapiric feeders (Peel et al., 1995), which may lie outside of the displayed profile.